Facile synthesis of black phosphorene via a low melting media assisted ball milling

Fengchen Zhou[a], Shaobo Li[a], Liuzhang Ouyang[a,b*], Jiangwen Liu[a], Jun Liu[a], Zhenguo Huang[*c], Min Zhu[a]

[a] School of Materials Science and Engineering, Guangdong Provincial Key Laboratory of Advanced Energy Storage Materials, South China University of Technology, Guangzhou, 510641, China

[b] China-Australia Joint Laboratory for Energy & Environmental Materials, Key Laboratory of Fuel Cell Technology of Guangdong Province, Guangzhou, 510641, China

[c] School of Civil and Environmental Engineering, University of Technology Sydney, NSW, 2007, Australia
* Corresponding Author:
Liuzhang Ouyang, E-mail: meouyang@scut.edu.cn
Zhenguo Huang, E-mail: zhenguo.huang@uts.edu.au

Abstract

Few-layer phosphorene (FLP) has attracted strong research interest due to its extraordinary physical and chemical properties. However, an efficient and rapid fabrication of high-quality FLP is still unavailable. Herein, a simple and efficient low melting media-assisted ball milling (LMMBM) approach is developed to prepare FLP in large quantities. The phase change of the LMM at higher temperatures leads to FLP with larger lateral dimensions compared to the ones obtained via dry solid state ball milling. Transmission electron microscope (TEM) studies indicated that liquid facilitates the slipping/curling of black phosphorus (BP) layers under the shearing force generated during ball milling. When used as an anode in Lithium-ion batteries, the FLP-C composite exhibits high initial Coulombic efficiency, stable cycling and rate capacity. This LMMBM approach can be adopted for mass production of other two-dimensional materials from their bulk counterparts.

Keywords: few-layer black phosphorus, phosphorene, ball milling, low melting media, Lithium-ion battery.

1. Introduction

Phosphorene has become the focus of research as a key member of the two-dimensional (2D) materials family, and its potential applications cover electronics, sensors, thermoelectric devices, energy conversion and storage, and biomedical devices [1-10]. Despite all the promising applications, it is still challenging to fabricate few-layer phosphorene (FLP) with high quality and in large quantities.

Nearly all the fabrication for 2D materials can be classified into two types: Top-down exfoliation and bottom-up growth. Compared with the "bottom-up" growth which typically requires special conditions such as high vacuum and high temperature, "top-down" method is more affordable and suitable for scale-up production of FLP from bulk black phosphorous (BP) [11-17]. Liquid ultrasonication has been employed to obtain FLP, but it is unsuitable for large-scale production since it takes a long time and the yield is low. Besides, the organic solvents (*e.g.* N-methyl-2-pyrrolidone, N,N-dimethylformamide) commonly used to exfoliate BP are high-boiling and toxic, which are difficult to remove and therefore affect the properties of FLP.

For practical applications, fabrication method featuring high yield, high efficiency, low cost, and good scalability, are needed. Ball milling is an established method for obtaining fine powders in different industries and has been used for preparing various 2D materials [18-22]. Milling agents (solvents or solid particles) have been introduced to improve the exfoliation efficiency by preventing the reaggregation of 2D materials, and sometimes to functionalize the obtained 2D materials as well. Lei *et al*. utilized urea-assisted mechanical exfoliation to fabricate functionalized few-layer h-BN with

an average thickness of 2.5 nm and lateral dimensions mostly below 100 nm [19]. By ball milling sucrose with h-BN, Chen *et al*. obtained sucrose-grafted h-BN nanosheets with a thickness of 4.4 nm and lateral size of 98 nm [20]. Assisted by urea, 18 kinds of MX_2 (M = Mo, W, V, Nb, Ta, Ti, and X = Te, Se, S) nanosheets were obtained via ball milling [21]. Although these ball milling processes with additives led to high yields, the average size of the obtained 2D materials is still far from satisfactory (less than 100 nm). Compared with dry milling, wet milling with the presence of solvents can produce nanosheets with larger sizes but the yield decreases due to the reduction in collision energy [22, 23]. Up to now, research on producing FLP by ball milling is still in its infancy.

Herein, for the first time, we report a simple and efficient approach to prepare FLP with a low melting media (urea-glocuse-NH_4Cl)-assisted ball milling (LMMBM). The urea-glocuse-NH_4Cl mixture melts at temperatures below 80 °C and produces a transparent solution due to hydrogen-bond interactions [24]. During ball milling, the collision energy prompts the melting of the urea-glocuse-NH_4Cl mixture, and the resultant solution alleviates the mechanical impact on the FLP basal area (preventing damaging the thin sheets) and also prevents 2D materials from reaggregation. To avoid toxic and high-boiling organic solvents, an ethanol (EtOH)-H_2O mixture (2:3 in volume) was chosen to disperse the FLP. The obtained FLP was tested as an anode material for Lithium-ion batteries and found to have excellent potential in energy storage application.

2. Experimental Section

2.1 Materials Preparation

The BP crystal was synthesized via chemical vapor transport (CVT) [25]. In brief, red phosphorus (0.5 g), Sn (20 mg), and SnI_4 (10 mg) were loaded in a silica tube with a length of 10 cm, inner diameter of 1.0 cm, and wall thickness of 0.2 cm. The tube was evacuated, sealed, and placed horizontally in a muffle furnace with one end closer to the heating elements. The temperature was increased to 650 °C and then dwelled for 2 h, and then slowly cooled to 480 °C over 10 h followed by natural cooling.

For a typical LMM-assisted ball milling exfoliation process, BP crystal (0.2 g) and LMM (urea-glocuse-NH_4Cl with 7:3:1 wt%, 1.1g) were added into a stainless steel jar filled with stainless steel balls (diameter of 6 mm, 50 g). The materials were ball milled for different times at 1000 rpm on a high-energy shaking mill (QM-3C, Nanjing Nada Instrument Co. Ltd.). The milled mixture was washed with deionized water and filtered through a nylon membrane (pore size=0.45 μm) to remove LMM, followed by dispersing into a EtOH-H_2O mixture (2:3 in volume) by bath sonication (400W, KQ-400KDE, Kunshan Ultrasonic Instruments, 40% power) for 1 h. The mixture was centrifuged at 3000 rpm for 30 min to remove the thick BP sheets. The supernatant was then filtered through a nylon membrane (pore size=0.2 μm) to collect powders, which were dried under vacuum to obtain the few-layer BP, noted as FLP-xh (x=milling time). The FLP-C and BP-C composites were also prepared by ball-milling. Specifically, FLP-7h or BP bulk was mixed with expanded graphite with a 7:3 weight ratio and the ball to powder weight ratio was 50:1.

2.2 Materials characterization

X-ray diffraction (XRD) data were collected on a PANalytical Empyrean diffractometer with Cu Kα radiation. Fourier-transform infrared spectroscopy (FTIR) data were obtained on Thermo Scientific Nicolet iS 50. Renishaw RM2000 confocal Raman microscope (with a laser of 532 nm) was used to obtain the Raman spectra. X-ray photoelectron spectroscopy (XPS) spectra were collected on Thermo Scientific ESCALAB 250. The morphologies were analyzed by scanning electron microscopy (SEM, Carl Zeiss Supra 40), transmission electron microscopy (TEM, JEOL JEM-2100), and atomic force microscopy (AFM, Bruker Dimension Icon).

2.3 Electrochemical measurements

The electrodes were fabricated by mixing active material (70 wt%), carboxymethyl cellulose (15 wt%) and Super P (15 wt%) in DI water to obtain a slurry, which was then coated on copper foils and dried overnight at 100 °C under vacuum. The test cells were assembled with lithium foils as the counter electrode in an argon-filled glove box. Electrolyte was a mixture of 1 M LiPF6 in EC/ DEC/DMC (1/1/1, v/v/v) with the addition of 10 wt% FEC. The charge/discharge tests were conducted on battery test systems (LAND CT2001A) with 0.01–2.00 V (vs. Li^+/Li) voltage window. The specific capacities were calculated according to the weight of active materials. Electrochemistry workstation (Gamry Interface 1000) was used for electrochemical

impedance spectroscopy (EIS, frequency between 100 kHz and 0.01 Hz) studies and cyclic voltammetry (CV, voltage window between 0.01-2.00 V) analysis.

3. Results and Discussion

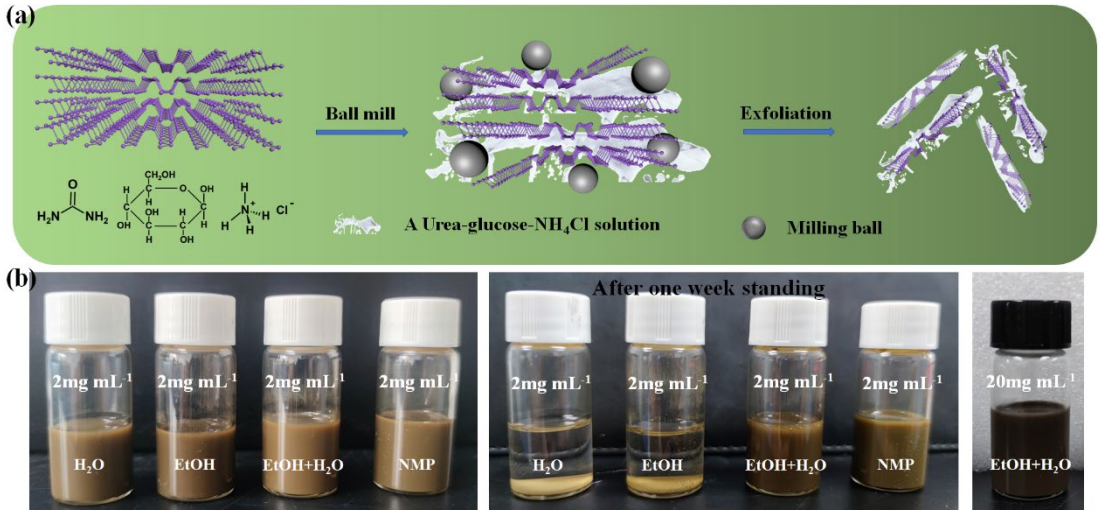

Fig. 1 (a) Schematic illustration of the exfoliation of FLP with LMMBM. (b) Digital photographs of FLP dispersed in different solvents: fresh (left), after one week standing (middle), and 20 mg mL^{-1} in EtOH-H_2O mixture (right).

Fig. 1a illustrates the LMMBM process schematically for preparing FLP with a low melting media (LMM, urea-glocuse-NH_4Cl) as the milling agent. Typically, 0.2 g bulk BP crystal (Fig. S1) and 1.1 g urea-glocuse-NH_4Cl (7:3:1, in weight ratio) were mixed and ball milled at 1000 rpm for different times. During ball milling, the collisions between the balls exfoliate the bulk BP to thin nanosheets. The low melting urea-glocuse-NH_4Cl solid mixture transforms into a liquid because of the local high temperature caused by collisions. The liquid would coat on the surface of FLP, which not only prevents the agglomeration of FLP, but also prevents it from being crushed

into smaller fragments since the liquid can buffer the mechanic impact. The milled products were dispersed in various solvents aided by sonication and then centrifuged to remove large BP particles. After filtering the supernatant and then washing the solid with water to remove the urea-glocuse-NH_4Cl agent, a gray product was obtained and denoted as FLP-*x* where *x* is the milling time in hour. The resultant FLP can be well dispersed in a wide range of solvents, such as a EtOH-H_2O mixture (2:3, in volume) and N-methyl-2-pyrrolidone (NMP), and the concentration can reach 20 mg mL^{-1} in the EtOH-H_2O mixture (Fig. 1b). The dispersion in certain solvents is stable up to one week without visible precipitation.

The produced FLP was characterized by scanning electron microscope (SEM), Raman spectroscopy, transmission electron microscope (TEM), and atomic force microscope (AFM). Taking FLP-7h as an example, FLP is smaller and thinner in comparison with the origin BP bulk powders. All the other FLP-x samples share similar morphology but with different lateral sizes and low yields (discussed in later section). To understand the role of LMM, two control experiments with/without the low melting media were carried out. One is ball milling BP without LMM followed by sonication and centrifugation using the same parameters. The obtained suspension (Fig. S2) after centrifugation appears almost translucent, which demonstrates an extremely low exfoliation efficiency. The other is ball milling BP with solid urea as the milling agent followed by sonication and centrifugation. Thin nanosheet structure was obtained but with smaller lateral sizes compared with LMM assisted exfoliation (as shown in Fig. S3). This demonstrates that the urea-glocuse-NH_4Cl mixture can facilitate the

exfoliation of BP flakes during ball milling, and the urea-glocuse-NH_4Cl solution can reduce the mechanic impact on the FLP and consequently leads to nanosheets with large lateral sizes. TEM image (Fig. 2b) shows the typical nanosheet structure. The lateral sizes vary from 110 to 250 nm and the average lateral size is 180 nm based on the statistics over a large amount of TEM images (Fig. 2c). HRTEM image (Fig. 2d) reveals a few atomic layers on the edges, and a well-ordered structure with a lattice spacing of 0.256 nm corresponding to the (111) planes of the BP crystal. The thickness of the FLP was further examined by AFM. As shown in Fig. 2e, the thickness of FLP-7h is between 4.51-7.67 nm corresponding to 7-15 layers, which is consistent with the HRTEM results. Raman spectra were collected to gather information on the structure and thickness of bulk BP and FLP (Fig. 2f). The A_g^1, B_{2g} and A_g^2 bands at 357.4, 431.7, 460 cm^{-1} correspond to out-of-plane mode, in-plane mode and vibration modes of BP crystal, respectively [26]. A clear blue-shift of A_g^2 peak indicates the reduction of the layer numbers of BP [15, 27]. All the results confirm the success in fabricating FLP using a low melting media as the milling agent.

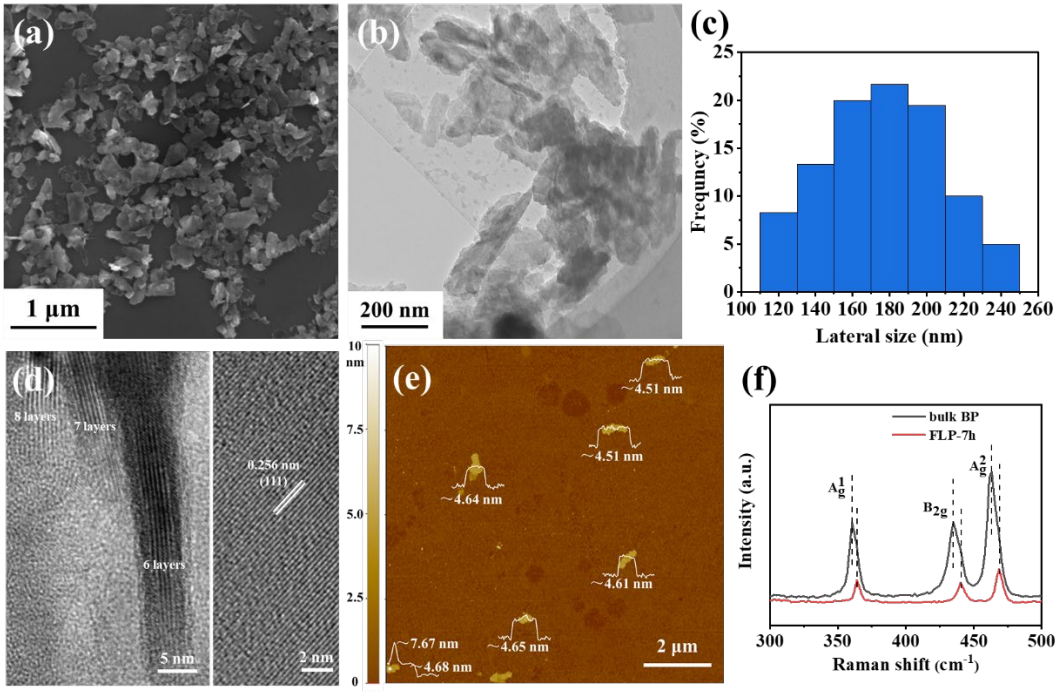

Fig. 2. Morphology, microstructure, and size distribution of the FLP-7h. (a) SEM image, (b) TEM image, (c) lateral size distribution, (d) HRTEM images of the edge and the center area, (e) AFM image and line scan profile of relative area, and (f) Raman spectra of bulk BP and FLP-7h.

Spectroscopic techniques confirm that the LMMBM-produced FLP has high purity without functional groups associated with glucose, urea and ammonium chloride. For example, Fourier-transform infrared (FTIR) analysis shows that the IR spectrum of the FLP-7h is similar to that of bulk BP (Fig. S4). Only P, O and C are observed in the full X-ray photoelectron spectroscopy (XPS) spectrum (Fig. S4), indicating the success in removing LMM from the product. XPS spectrum of P2p shows a pair of peaks at 129.8 and 130.6 eV corresponding to 2p3/2 and 2p1/2. Another broad peak at 134.2 eV is assigned to oxidized P [28, 29]. These results indicate that FLP is free of chemicals

used in the fabrication, which can be critical for certain applications such as electronics and biomedical devices.

To understand the exfoliation process, TEM images of the BP powders ball milled for 7 h were collected (Fig. 3). Fig. 3a shows few-layer BP (region i) slipping from bulk BP (region iii), similar to TEM observation of exfoliated h-BN [30]. Fig. 3b shows a few-layer BP bending away from each other, similar to an *in-situ* TEM study revealing the bending of few-layer MoS_2 sheets from mother MoS_2 under shear forces [31]. Fig. 3c shows several two-layer BP nanosheets sliding off each other. The upper right inset shows the schematic illustration of the structure, and the bottom left inset is a HRTEM image with the (020) and (111) fringes. Fig. 3d shows the schematic illustration of two exfoliating processes: sliding and bending. At the start of ball milling, the shear force causes the top layers of bulk BP to slide. With the ball milling process continuing, solid urea-glucose-NH_4Cl melts as the internal and local temperatures increase due to mechanic collisions. The small liquid molecules can play three roles in the formation of few-layer BP nanosheets. First, they can enter into the cracks between the layers and weaken interactions between them and facilitate exfoliation. Second, liquid coating on FLP buffers the mechanic impact and therefore alleviates otherwise continuous fragmentation of FLP. Third, the LMM solution on the surface of FLP prevents the agglomeration of FLP. Noted that once melted the LMM maintains its liquid state even at room temperature, and therefore the ball milled product appears viscous (Fig. 3e). Milling time apparently affects the morphology of the product. With a ball milling of 5h, the product exhibits nanosheet structure with thickness smaller than 10 nm and

average lateral size around 220 nm (Fig.S5 a-d). When increasing to 10 h, the thickness is similar, but the average lateral size decreases dramatically to only around 110 nm. Therefore, to obtain FLP with large lateral size, the milling time of 7h was chosen to produce FLP for further analysis. The yield of LMMBM method for 7 h is 35.3%, which is higher than those of liquid ultrasonication method as reported in Chen's work (30% for 20 h) and Sun's work (17% for 10 h) [32, 33]. To verify the LMMBM strategy, a planet ball-mill (with a ball to sample weight ratio of 50:1 at 500 rpm) was also employed to synthesized FLP. From the results as shown Fig. S6, FLP can be obtained but its yield needs to be optimized.

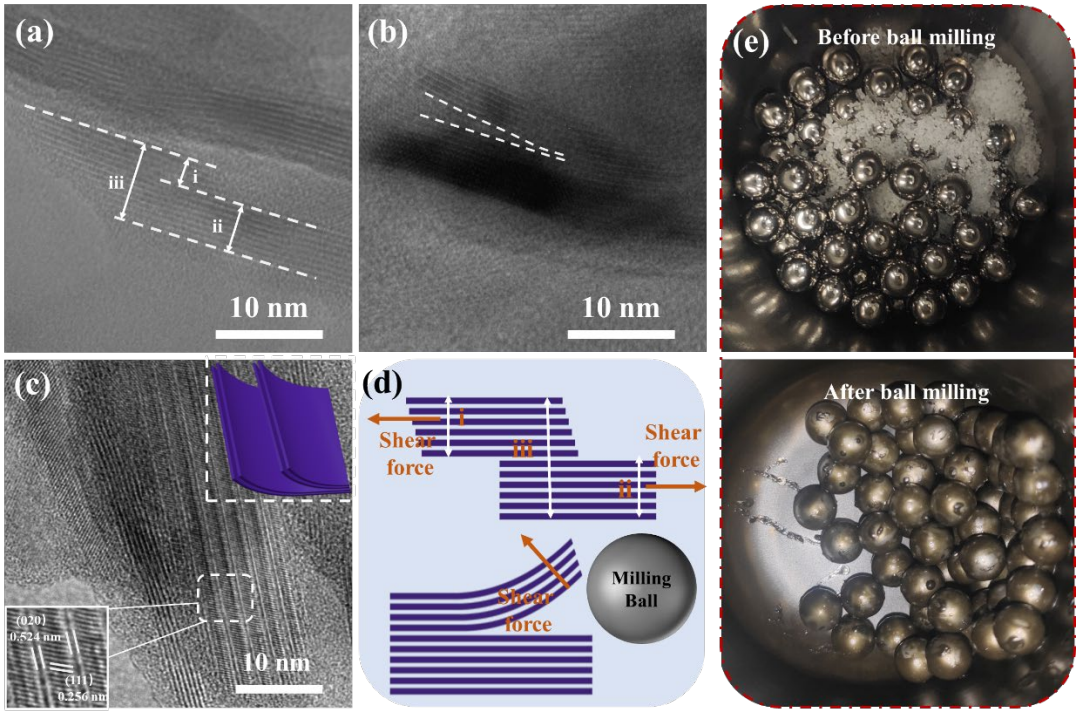

Fig.3 (a) SEM image showing one region sliding from another, (b) splitting and bending of FLP, (c) two-layer BP nanosheets sliding off each other, (d) Illustration of the sliding

and bending during the ball milling, and (e) digital images of the powders before and after ball milling (without any treatment).

BP is considered as a promising anode material for lithium ion batteries due to its suitable reaction potential and high theoretical specific capacity of 2596 mAh g^{-1} [34]. However, bulk BP exhibits poor cycling performance owing to its low electronic conductivity, slow Li^+ diffusion and large volume expansion during electrochemical reaction [16, 35]. FLP has therefore been explored since it exhibits shorter Li^+ diffusion path and larger active surface area compared with bulk BP [34, 35]. Accordingly, FLP-7h with expanded graphite (noted as FLP-C composite, as shown Fig.S7) was prepared as anode material in Li-ion batteries. For comparison, bulk BP mixed with expanded graphite (noted as BP-C composite) was tested as well.

Fig. 4a shows the initial charge-discharge curves of the FLP-C and BP-C electrodes at a current density of 500 mAh g^{-1}. The initial discharge specific capacity of FLP-C electrode is 1900.3 mAh g^{-1} with a Coulombic efficiency of 89.2%, which is slightly lower than that of the BP-C electrode (1964.7 mAh g^{-1} with the initial Coulombic efficiency of 92.1%). The lower discharge capacity and initial Coulombic efficiency of the FLP-C electrode is mainly due to the oxidation of FLP (Fig. S4). The hysteresis of the discharge/charge voltage of FLP-C was determined to be 0.311 V, which is smaller than that of BP-C electrode (0.398 V). This result indicates that the FLP-C electrode has a smaller polarization due to the fast Li-ion transport and enhanced electron migration enabled by higher surface area and smaller sizes of the flakes. Fig.

4b shows the CV curves of FLP-C electrode at a scan rate of 0.2 mV s^{-1} between 0.01 and 2.0 V. During the initial cathodic scan, a peak appeared at 0.5 V which corresponds to the formation of Li_xP (x = 1-3) [36]. On the anodic scan, a peak at 1.03 V appeared which is associated with the delithiation process of Li_xP. This anodic peak split into two peaks, around 1.0 and 1.12 V, respectively, during the subsequent cycles, indicating a stepwise delithiation process from Li_xP to P [37, 38]. However, the integral area of the anodic peak remains the same during the cycling, which indicates an excellent reversibility of the electrochemical reaction of FLP-C electrode.

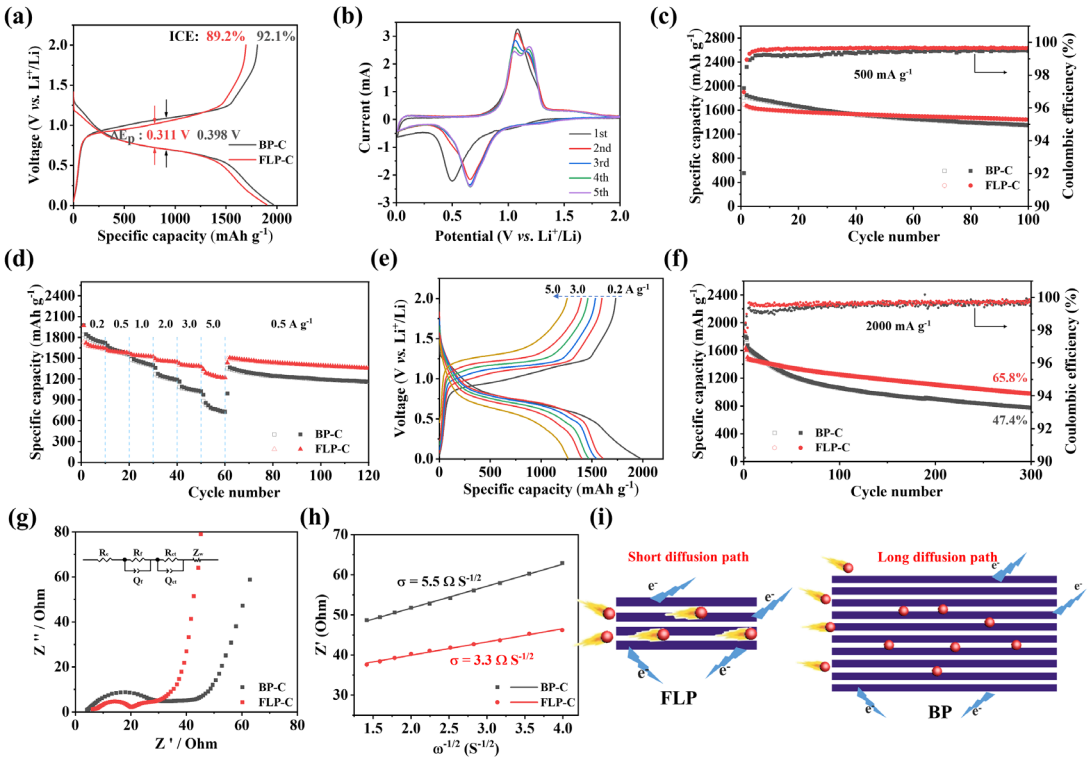

Fig. 4 (a) Charge-discharge curves of the initial cycle of FLP-C and BP-C electrodes, (b) CV curves of FLP-C electrode at a scan rate of 0.2 mV s^{-1} between 0.01 and 2.0 V, (c) cycle performances at 500 mA g^{-1}, (d) rate performance, (e) the charge/discharge curves of FLP-C electrode at different current densities, (f) cycle performances and coulombic efficiency at 2000 mA g^{-1}, (g) electrochemical impedance spectra of FLP-C

and BP-C electrodes after 50 cycles at a discharge state of 0.01V, (h) relationship between Z_{re} and $\omega^{-1/2}$, and (i) the proposed mechanism of Li^+ diffusion in FLP-C and BP-C electrodes.

Fig. 4c shows the cycling performance and Columbic efficiency of FLP-C and BP-C electrodes at a current density of 500 mA g^{-1}. The FLP-C electrode exhibits a stable cycling performance, and a reversible specific capacity of 1440 mAh g^{-1} can be achieved at the 100th cycle, with a capacity retention of 84.9%. In contrast, the cycling performance of BP-C electrode shows a continuous fading, and a reversible capacity of 1344.4 mAh g^{-1} was delivered at the 100th cycle with a capacity retention of 74.4%. The Coulombic efficiency of FLP-C can be maintained at 99.6% during cycling, which is also higher than that of BP-C electrode (99.2%). The low Coulombic efficiency of BP-C can be due to lithium trapped inside the large BP flakes. Furthermore, the large size of BP always faces severe volume expansion, resulting in the pulverization of particles and therefore poor electronic contact. The volume expansion will also expose more active electrolyte/electrode interfaces, accelerating the electrolyte decomposition.

Fig. 4d shows the rate performance of FLP-C and BP-C electrodes at different current densities. The FLP-C electrode exhibits an average specific capacity of 1663.9, 1585.1, 1529.4, 1455 and 1390.5 mAh g^{-1} at 0.2, 0.5,1.0, 2.0 and 3.0 A g^{-1}, respectively. Even at a high current density of 5.0 A g^{-1}, an average specific capacity of 1250.7 mAh g^{-1} can be achieved, with a capacity retention of 75.2% based on the capacity at 0.2A g^{-1}. In contrast, although the BP-C electrode exhibits a higher capacity than FLP-C at the

lower current density, only 777.8 mAh g^{-1} can be obtained at 5.0 A g^{-1}, indicating inferior Li^+ diffusion and lower electrochemical reaction kinetics in BP-C composite. Moreover, the FLP-C electrode can achieve a high capacity of 1491.2 mAh g^{-1} once returning to 0.5 A g^{-1} after ultrahigh rate cycling, featuring stable cycling for another 60 cycles without obvious fading. The charge/discharge profiles of FLP-C electrode show a small voltage hysteresis and clear charge/discharge voltage platform with the increase in current density (Fig. 4e), which also demonstrate an excellent rate performance of FLP-C electrode. Besides, the FLP-C electrode also exhibits a high capacity retention of about 65.8% (based on the 4^{th} cycle) after 300 cycles with the Columbic efficiency maintaining at 99.7% (Fig. 4f). In contrast, the BP-C electrode shows a lower capacity retention of 47.4% (based on the 4^{th} cycle) after 300 cycles and the Columbic efficiency maintained at only 99.1% during the initial 50 cycles. Compared with reported P-based composites used for batteries (Table S1), the prepared FLP-C electrode in the present work shows excellent rate capability and high specific capacity.

The reaction kinetics of two electrodes were evaluated by EIS analysis, as shown in Fig. 4g. The Nyquist plots consist of the SEI resistances (R_f), charge transfer resistances (R_{ct}), and Li^+ diffusion process. Based on the equivalent circuit given in the inset, the FLP-C electrode has a lower R_{ct} parameter than the BP-C electrode after 50 cycles, which favors fast reaction kinetic of FLP-C electrode. The Warburg coefficient σ (Fig. 4h) was determined from the slope of the Warburg plot between Z_{re} and $\omega^{-1/2}$ [39]. The FLP-C electrode shows a smaller σ value, suggesting a superior ionic

diffusion. The resistance and Li^+ ion diffusion difference can be reasoned with the electron and ionic transfer pathway in the composite, as illustrated in Fig. 4i. FLP has a smaller layer number and lateral size which shorten the electron and ion transfer paths, and therefore leads to the smaller charge transfer resistance and faster Li^+ ion diffusion.

4. Conclusion

We demonstrate a low melting media (urea-glocuse-NH_4Cl)-assisted ball milling process to fabricate few-layer phosphorene (FLP) nanosheets. Ball milling generates shearing force on the surface of bulk BP, which helps to split and curl BP atomic layers. Rise in temperature due to mechanic collisions converts the solid LMM to liquid media. The liquid coating on the atomic layers reduces mechanic impact and thus protect FLP from excessive damage, and also prevents reaggregation of the FLP. The lateral dimension of FLP is around 180 nm with an average thickness of 4-5 nm. Used as the anode for LIBs, the FLP-C composites deliver high initial Coulombic efficiency of 89.2%, stable specific capacity of 1440 mAh g^{-1} after 100 cycles, and excellent rate capacity of 1250.7 mAh g^{-1} at 5 A g^{-1}. Compared with other methods to fabricate 2D materials, this LMM-assisted ball-milling is contamination free and conducive to large lateral sizes. We believe it is applicable to large-scale exfoliation of other 2D materials.

Acknowledgments

This work was financially supported by the Foundation for Innovative Research Groups of the National Natural Science Foundation of China (No. NSFC51621001). Z.H. acknowledges support under the Australian Research Council's (ARC) Discovery Future Fellowship (FT190100658).

References

[1] L.K. Li, Y.J. Yu, G.J. Ye, Q.Q. Ge, X.D. Ou, H. Wu, D.L. Feng, X.H. Chen, Y.B. Zhang, Black phosphorus field-effect transistors, Nat. Nanotechnol. 9 (2014), 372-377.

[2] J. Na, Y.T. Lee, J.A. Lim, D.K. Hwang, G.-T. Kim, W.K. Choi, Y.-W. Song, Few-layer black phosphorus field-effect transistors with reduced current fluctuation, ACS Nano 8 (2014), 11753-11762.

[3] M. Akhtar, G. Anderson, R. Zhao, A. Alruqi, J.E. Mroczkowska, G. Sumanasekera, J.B. Jasinski, Recent advances in synthesis, properties, and applications of phosphorene, Npj 2d Mater. Appl. 1 (2017).

[4] J. Pang, A. Bachmatiuk, Y. Yin, B. Trzebicka, L. Zhao, L. Fu, R.G. Mendes, T. Gemming, Z. Liu, M.H. Rummeli, Applications of phosphorene and black phosphorus in energy conversion and storage devices, Adv. Energy Mater. (2017), 1702093.

[5] Y. Zhang, Y. Zheng, K. Rui, H.H. Hng, K. Hippalgaonkar, J. Xu, W. Sun, J. Zhu, Q. Yan, W. Huang, 2D Black phosphorus for energy storage and thermoelectric applications, Small 13 (2017), 1700661.

[6] H. Liu, K. Hu, D. Yan, R. Chen, Y. Zou, H. Liu, S. Wang, Recent advances on black phosphorus for energy storage, catalysis, and sensor applications, Adv. Mater. 30 (2018), 1800295.

[7] M. Qiu, W.X. Ren, T. Jeong, M. Won, G.Y. Park, D.K. Sang, L.P. Liu, H. Zhang, J.S. Kim, Omnipotent phosphorene: a next-generation, two-dimensional nanoplatform for multidisciplinary biomedical applications, Chem. Soc. Rev. 47 (2018), 5588-5601.

[8] H. Jin, S. Xin, C. Chuang, W. Li, H. Wang, J. Zhu, H. Xie, T. Zhang, Y. Wan, Z. Qi, W. Yan, Y.R. Lu, T.S. Chan, X. Wu, J.B. Goodenough, H. Ji, X. Duan, Black phosphorus composites with engineered interfaces for high-rate high-capacity lithium storage, Science 370 (2020), 192-197.

[9] J. Mei, Y.W. Zhang, T. Liao, X.M. Peng, G.A. Ayoko, Z.Q. Sun, Black phosphorus nanosheets promoted 2D-TiO_2-2D heterostructured anode for high-performance lithium storage, Energy Storage Mater. 19 (2019), 424-431.

[10] X. Ren, J. Zhou, X. Qi, Y. Liu, Z. Huang, Z. Li, Y. Ge, S.C. Dhanabalan, J.S. Ponraj, S. Wang, J. Zhong, H. Zhang, Few-layer black phosphorus nanosheets as electrocatalysts for highly efficient oxygen evolution reaction, Adv. Energy Mater. (2017), 1700396.

[11] J.L. Zhang, C. Han, Z.H. Hu, L. Wang, L. Liu, A.T.S. Wee, W. Chen, 2D Phosphorene: epitaxial growth and enterface engineering for electronic devices, Adv. Mater. 30 (2018), 1802207.

[12] A.E. Del Rio Castillo, V. Pellegrini, H. Sun, J. Buha, D.A. Dinh, E. Lago, A. Ansaldo, A. Capasso, L. Manna, F. Bonaccorso, Exfoliation of few-layer black phosphorus in low-boiling-point solvents and its application in Li-ion batteries, Chem. Mater. 30 (2018), 506-516.

[13] D. Hanlon, C. Backes, E. Doherty, C.S. Cucinotta, N.C. Berner, C. Boland, K. Lee, A. Harvey, P. Lynch, Z. Gholamvand, S. Zhang, K. Wang, G. Moynihan, A. Pokle, Q.M. Ramasse, N. McEvoy, W.J. Blau, J. Wang, G. Abellan, F. Hauke, A. Hirsch, S. Sanvito, D.D. O'Regan, G.S. Duesberg, V. Nicolosi, J.N. Coleman, Liquid exfoliation of solvent-stabilized few-layer black phosphorus for applications beyond electronics, Nat. Commun. 6 (2015), 8563.

[14] J. Sun, H.W. Lee, M. Pasta, H. Yuan, G. Zheng, Y. Sun, Y. Li, Y. Cui, A phosphorene-graphene hybrid material as a high-capacity anode for sodium-ion batteries, Nat. Nanotechnol. 10 (2015), 980-985.

[15] A. Ambrosi, Z. Sofer, M. Pumera, Electrochemical exfoliation of layered black phosphorus into phosphorene, Angew. Chem. Int. Ed. 56 (2017), 10443-10445.

[16] W. Zheng, J. Lee, Z.W. Gao, Y. Li, S. Lin, S.P. Lau, L.Y.S. Lee, Laser-assisted ultrafast exfoliation of black phosphorus in liquid with tunable thickness for Li-ion batteries, Adv. Energy Mater. (2020) 1903490.

[17] H. Huang, M. Gao, Y. Kang, J. Li, J. Wang, L. Wu, P.K. Chu, Y. Huang, M.R. Ibarra, X.F. Yu, Rapid and scalable production of high-quality phosphorene by plasma-liquid technology, Chem. Commun. 56 (2019), 221-224.
[18] W.F. Zhao, M. Fang, F.R. Wu, H. Wu, L.W. Wang, G.H. Chen, Preparation of graphene by exfoliation of graphite using wet ball milling, J Mater. Chem. 20 (2010), 5817-5819.
[19] W. Lei, V.N. Mochalin, D. Liu, S. Qin, Y. Gogotsi, Y. Chen, Boron nitride colloidal solutions, ultralight aerogels and freestanding membranes through one-step exfoliation and functionalization, Nat. Commun. 6 (2015), 8849.
[20] S. Chen, R. Xu, J. Liu, X. Zou, L. Qiu, F. Kang, B. Liu, H.M. Cheng, Simultaneous production and functionalization of boron nitride nanosheets by sugar-assisted mechanochemical exfoliation, Adv. Mater. 31 (2019), 1804810.
[21] L. Zhang, C. Chen, J. Zhou, G. Yang, J. Wang, D. Liu, Z. Chen, W. Lei, Solid phase exfoliation for producing dispersible transition metal dichalcogenides nanosheets, Adv. Funct. Mater. 30 (2020), 2004139.
[22] X. Li, J. Shen, C. Wu, K. Wu, Ball-mill-exfoliated graphene: tunable electrochemistry and phenol sensing, Small 15 (2019), 1805567.
[23] D. Lee, B. Lee, K.H. Park, H.J. Ryu, S. Jeon, S.H. Hong, Scalable exfoliation process for highly soluble boron nitride nanoplatelets by hydroxide-assisted ball milling, Nano Lett. 15 (2015), 1238-1244.
[24] L.V. Theresa, M. Shaibuna, K. Sreekumar, Glucose:urea:NH_4Cl low melting mixture for the synthesis of symmetric azines, Synth. Commun. 49 (2019), 3148-3160.
[25] M. Köpf, N. Eckstein, D. Pfister, C. Grotz, I. Krüger, M. Greiwe, T. Hansen, H. Kohlmann, T. Nilges, Access and in situ growth of phosphorene-precursor black phosphorus, J. Cryst. Growth 405 (2014), 6-10.
[26] M. Zhao, H. Qian, X. Niu, W. Wang, L. Guan, J. Sha, Y. Wang, Growth mechanism and enhanced yield of black phosphorus microribbons, Cryst. Growth Des. 16 (2016), 1096-1103.
[27] Z. Guo, H. Zhang, S. Lu, Z. Wang, S. Tang, J. Shao, Z. Sun, H. Xie, H. Wang, X.-F. Yu, P.K. Chu, From black phosphorus to phosphorene: basic solvent exfoliation, evolution of raman scattering, and applications to ultrafast photonics, Adv. Funct. Mater. 25 (2015), 6996-7002.
[28] J. Sun, G. Zheng, H.W. Lee, N. Liu, H. Wang, H. Yao, W. Yang, Y. Cui, Formation of stable phosphorus-carbon bond for enhanced performance in black phosphorus nanoparticle-graphite composite battery anodes, Nano Lett. 14 (2014), 4573-4580.
[29] W.-J. Li, S.-L. Chou, J.-Z. Wang, H.-K. Liu, S.-X. Dou, Significant enhancement of the cycling performance and rate capability of the P/C composite via chemical bonding (P-C), J. Mater. Chem. A 4 (2016), 505-511.
[30] C. Zhang, J. Tan, Y. Pan, X. Cai, X. Zou, H.M. Cheng, B. Liu, Mass production of 2D materials by intermediate-assisted grinding exfoliation, Natl. Sci. Rev. 7 (2020), 324-332.
[31] D.M. Tang, D.G. Kvashnin, S. Najmaei, Y. Bando, K. Kimoto, P. Koskinen, P.M. Ajayan, B.I. Yakobson, P.B. Sorokin, J. Lou, D. Golberg, Nanomechanical cleavage of molybdenum disulphide atomic layers, Nat. Commun. 5 (2014), 3631.
[32] L. Chen, G. Zhou, Z. Liu, X. Ma, J. Chen, Z. Zhang, X. Ma, F. Li, H.M. Cheng, W. Ren, Scalable clean exfoliation of high-quality few-layer black phosphorus for a flexible lithium ion battery, Adv. Mater. 28 (2016), 510-517.
[33] J. Sun, H.W. Lee, M. Pasta, H. Yuan, G. Zheng, Y. Sun, Y. Li, Y. Cui, A phosphorene-graphene hybrid material as a high-capacity anode for sodium-ion batteries, Nat. Nanotechnol. 10 (2015), 980-985.

[34] L. Chen, G. Zhou, Z. Liu, X. Ma, J. Chen, Z. Zhang, X. Ma, F. Li, H.M. Cheng, W. Ren, Scalable clean exfoliation of high-quality few-layer black phosphorus for a flexible lithium ion battery, Adv. Mater. 28 (2016), 510-517.
[35] H. Jin, H. Wang, Z. Qi, D.S. Bin, T. Zhang, Y. Wan, J. Chen, C. Chuang, Y.R. Lu, T.S. Chan, H. Ju, A.M. Cao, W. Yan, X. Wu, H. Ji, L.J. Wan, A black phosphorus-graphite composite anode for Li-/Na-/K-ion batteries, Angew. Chem. Int. Ed. 59 (2020), 2318-2322.
[36] T. Yuan, J. Ruan, C. Peng, H. Sun, Y. Pang, J. Yang, Z.-F. Ma, S. Zheng, 3D red phosphorus/sheared CNT sponge for high performance lithium-ion battery anodes, Energy Storage Mater. 13 (2018), 267-273.
[37] W.C. Chang, K.W. Tseng, H.Y. Tuan, Solution synthesis of iodine-doped red phosphorus nanoparticles for lithium-ion battery anodes, Nano Lett. 17 (2017), 1240-1247.
[38] Z. Yu, J. Song, M.L. Gordin, R. Yi, D. Tang, D. Wang, Phosphorus-graphene nanosheet hybrids as lithium-ion anode with rxceptional high-temperature cycling stability, Adv. Sci. 2 (2015), 1400020.
[39] Z.L. Li, H.L. Zhao, P.P. Lv, Z.J. Zhang, Y. Zhang, Z.H. Du, Y.Q. Teng, L.N. Zhao, Z.M. Zhu, Watermelon-like structured SiO_x-TiO_2@C nanocomposite as a high-performance lithium-ion battery anode, Adv. Funct. Mater. 28 (2018), 1605711.